



Particle clustering and dispersion in dense turbulent interfacial suspensions

Seunghwan Shin¹ , Laura Stricker² and Filippo Coletti¹

¹Department of Mechanical and Process Engineering, ETH Zurich, Zurich 8092, Switzerland

²Institute of Process Engineering, Otto von Guericke University, 39106 Magdeburg, Germany

Corresponding author: Seunghwan Shin, seshin@ethz.ch

(Received 9 December 2024; revised 25 March 2025; accepted 28 April 2025)

We investigate suspensions of non-Brownian, millimetric monodisperse spherical particles floating at quasi-two-dimensional fluid interfaces, from dilute to dense concentrations. Building upon the phase diagram in the capillary number (Ca) and areal fraction (ϕ) constructed by Shin & Coletti (2024 *J. Fluid Mech.* **984**, R7), we analyse the dynamics of both aggregation and dispersion. In the capillary-driven clustering regime ($Ca < 1$), strong inter-particle bonds yield large, fractal-like clusters that grow by hit-and-stick collisions. In the drag-driven break-up regime ($Ca > 1$, $\phi < 0.4$), turbulent fluctuations overcome capillarity and result in particles moving similarly to passive tracers and forming clusters by random adjacency. In the lubrication-driven clustering regime ($Ca > 1$, $\phi > 0.4$), the close inter-particle proximity amplifies lubrication forces and results in large, crystal-like clusters. Above a threshold concentration that depends on Ca , self-similar percolating clusters span the entire domain. The particle transport exhibits a classic ballistic-to-diffusive transition, with the long-time diffusivity hindered by the reduced fluctuating energy at high concentrations. Nearby particles separate at initially slow rates due to strong capillary attraction, and then follow a super-diffusive dispersion regime. In dense suspensions, the process is characterised by the time scale associated with inter-particle collisions and by the energy dissipation rate defined by the lubrication force between adjacent particles. Our results provide a framework for predicting particle aggregation in interfacial suspensions such as froth flotation and pollutant dispersion, and may inform the design of advanced materials through controlled colloidal self-assembly.

Key words: particle/fluid flow, suspensions

1. Introduction

Dense turbulent suspensions play a pivotal role in a wide range of industrial applications and natural phenomena such as pneumatic conveying, debris flow, sediment transport and snow avalanches. Here, we term a suspension ‘dense’ when inter-particle interactions are frequent compared with the typical response time of the particles, and ‘dilute’ otherwise (Clift, Grace & Weber 2005). Despite their prevalence, understanding these complex systems remains elusive due to the intricate interplay of multiple physical mechanisms across different scales. Traditionally, research studies have focused on either dense, viscous suspensions (Guazzelli, Morris & Pic 2011) or dilute, turbulent ones (Balachandar & Eaton 2010). The study of dense turbulent suspensions has been thwarted by the physical complexities that arise when both inertial effects and inter-particle interactions are combined, and by the difficulty of both measuring and simulating the system behaviour. Recent advances in experimental methods (e.g. refractive index matching and medical imaging) and numerical models (such as particle-resolved simulations) have enabled the investigation of transitional and turbulent dense suspensions, for example in pipe flows (Matas, Morris & Guazzelli 2003; Hogendoorn & Poelma 2018; Agrawal, Choueiri & Hof 2019; Hogendoorn *et al.* 2023), channel flows (Picano, Breugem & Brandt 2015; Wang *et al.* 2016; Zade *et al.* 2018; Olivieri *et al.* 2020; Fong & Coletti 2022), boundary layers (Baker & Coletti 2019), decaying turbulence (Zhang & Rival 2018) and sediment transport (Vowinkel *et al.* 2023). The nature of the methodologies, however, entails limitations on the accessible regimes, specifically on the particle properties and concentration, and on the system scale. Thus, while progress is fast, the area can still be considered in its infancy.

An additional layer of complexity arises when particles are confined at fluid interfaces, where their dynamics differs substantially from that in the bulk (Singh & Joseph 2005; Madivala, Fransaer & Vermant 2009; Magnaudet & Mercier 2020). Previous studies exploring the behaviour of particles at interfaces have mostly focused on low-inertia or microscopic colloidal systems (Hoekstra *et al.* 2003; Fuller & Vermant 2012; Garbin 2019). On the other hand, dense turbulent interfacial suspensions are present in both industrial and natural settings, for example froth flotation in process engineering and in patches of marine plastics. Multiple mechanisms may then superpose; for example, particle clustering may manifest itself due to hydrodynamic interactions (Brown & Jaeger 2014), inertial effects (Brandt & Coletti 2022) and capillarity (Protière 2023).

In our prior work (Shin & Coletti 2024), we examined the interactions of non-Brownian, monodisperse spherical particles at the interface of quasi-two-dimensional (Q2-D) turbulent liquid layers. By systematically varying parameters such as turbulence intensity, interfacial tension, particle size and concentration, we investigated the clustering propensity, cluster size and the particles’ mean kinetic energy, all influenced by the interplay of capillarity, drag and lubrication forces. The balance of these forces was quantified by two key non-dimensional parameters: the capillary number (Ca) and the areal fraction (ϕ). The former is the ratio between the drag force pulling nearby particles apart and the capillary attraction keeping them together. The latter is related to the ratio between the footprint of all particles in the domain and the area of the same domain. We proposed a phase diagram identifying three distinct regimes in the $Ca - \phi$ space, each associated with a different clustering behaviour and kinetic energy of the particles.

Building on this foundation, the present study explores in detail the individual and collective particle dynamics within these regimes. By analysing the spatio-temporal scales and structure of clusters as well as the Lagrangian particle motion, we elucidate the underlying mechanisms governing the aggregation and dispersion in the various regimes. The paper is organised as follows. Section 2 presents the experimental set-up, defines the physical parameters and describes the measurement approach and data processing.

Label	ρ_p [g cm ⁻³]	d_p [mm]	d_p/η	Re	Re_α	ϕ	Ca	St	Bo
SL	1.0	1.09 ± 0.07	0.99–2.14	566–1747	4.7–14.2	0.01–0.43	0.09–0.29	0.03–0.09	3.3 × 10 ⁻³
DL1	1.0	1.09 ± 0.07	0.57–2.10	229–1035	5.8–21.8	0.14–0.44	0.41–1.84	0.01–0.06	6.9 × 10 ⁻³
DL2	0.96	1.84 ± 0.17	0.97–3.54	192–1047	4.9–22.2	0.08–0.71	0.33–2.69	0.03–0.15	2.9 × 10 ⁻²

Table 1. Summary of the experimental parameters.

Section 3 discusses the results in terms of cluster properties (3.1) and particle motion (3.2). Section 4 draws conclusions and offers an outlook for future work.

2. Methods

We use a conductive fluid consisting of a 10% CuSO₄ aqueous solution by mass, with density $\rho_f = 1.08 \text{ g ml}^{-1}$ and kinematic viscosity $\nu = 1.0 \times 10^{-6} \text{ m}^2 \text{ s}^{-1}$. The conductive fluid is contained in a $320 \times 320 \text{ mm}^2$ tray, placed above an 8×8 magnet array arranged in a checkerboard pattern with alternating polarities. The flow is induced by applying DC current through copper electrodes at opposite sides of the tray, generating Lorentz forces in the horizontal direction. The magnets are spaced at a centre-to-centre distance of 35 mm, defining the forcing scale L_F . This set-up aligns with configurations frequently employed in prior Q2-D turbulence studies, and was detailed extensively in our previous study (Shin, Coletti & Conlin 2023).

We employ two distinct fluid layer set-ups and two sizes of polyethylene spheres (Cospheric WPMS-1.00, CPB-0.96). The set-ups include: a single-layer (SL) configuration, where spheres are placed at the free surface of a 7 mm-deep conductive layer: and double-layer (DL) configurations (DL1 and DL2), with a 2 mm-thick mineral oil layer on top of an 8 mm-thick conductive layer, where the spheres are at the liquid–liquid interface. In DL1 and DL2 the fluid layers are identical, but different particle sizes are used. Particles are introduced in varying quantities to adjust the areal fraction $\phi \equiv N_p(\pi d_p^2/4)/A_{FOV}$, where N_p is the time-averaged number of particles in the field of view of area A_{FOV} , and d_p is the particle diameter. To explore the full range of concentrations from fully dilute to fully dense, we vary ϕ from 1% to 71%.

To ensure consistency across experiments, we verify that the Bond number (Bo) and the Stokes number (St) are both much smaller than 1 in all cases. The small Bond number, $Bo \equiv (\rho_f - \rho_p)gd_p^2/(4\gamma)$, with ρ_p the particle density, g is the gravitational acceleration and γ the interfacial tension, indicates that interfacial distortion due to buoyancy is negligible. The small Stokes number, $St \equiv \tau_p u_{rms,f}/L_F$, where $\tau_p = \rho_p d_p^2/(18\mu)$ is the particle response time, μ is the dynamic viscosity of the carrying fluid (or simply fluid viscosity) and $u_{rms,f}$ is the root-mean-square velocity of the flow $u_{rms,f} = \langle \mathbf{u}(\mathbf{x}, t) \cdot \mathbf{u}(\mathbf{x}, t) \rangle_{x,t}^{1/2}$, indicates that particle inertia is insignificant in comparison with the energetic flow scales, justifying the assumption of a Stokesian dynamics. The capillary number is defined as $Ca \equiv 6\sqrt{2}\pi d_p^6 u_{rms,f}/(\Theta L_F)$, where $\Theta = 12\gamma h_{qp}^2 d_p^3/\mu$, with γ the interfacial tension and h_{qp} the amplitude of the quadrupole mode of the interfacial distortion, whose measurement was discussed in our previous study (Shin & Coletti 2024). Note that our formulation of Ca is based on an average extensional strain rate evaluated at a characteristic particle separation; therefore, an increase in Ca indicates that, on average, viscous (or turbulent) drag increasingly overcomes capillary forces, resulting in diminished particle cohesion. Further details of the experimental parameters are provided in table 1.

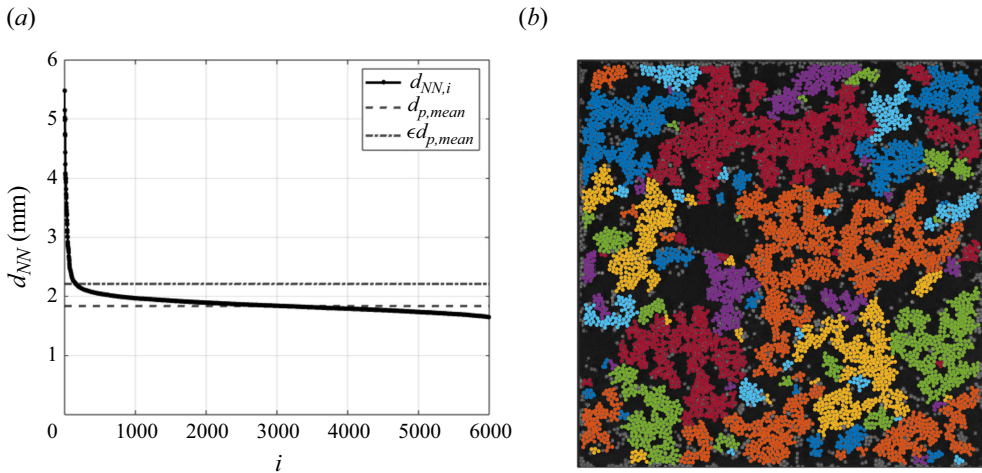


Figure 1. Choice of a searching radius. (a) Distance to the nearest neighbour d_{NN} sorted in descending order. The dashed line represents the mean particle diameter (d_p), and the dash-dot line indicates the cutoff distance used to identify clustered neighbours. (b) An example of cluster detection from the corresponding experiment at $Ca = 0.33$ and $\phi = 0.44$. Particles within the same cluster are indicated with the same colour.

We use a Phantom VEO 640 CMOS camera to record 100-second sequences at rates of 100–240 frames per second, ensuring that inter-frame particle displacements are confined to approximately 5 pixels or ~ 1 mm. The imaging focuses on the central zone of the tray, approximately L_F away from its boundaries, to minimise edge effects. The field of view captures a spatially and temporally homogeneous system of particles, with temporal fluctuations in the number of imaged particles typically smaller than 1% of the mean. Particle centroids are tracked with sub-pixel accuracy using an in-house code, allowing us to reconstruct their Lagrangian trajectories. We define clusters as groups of adjacent particles. For their identification we employ the Density-Based Spatial Clustering of Applications with Noise (DBSCAN) algorithm (Ester *et al.* 1996), setting a search radius around each particle centroid to determine adjacency, with a minimum requirement of four neighbours. This is preferred to cluster identification strategies as the Voronoi tessellation (Baker *et al.* 2017; Liu *et al.* 2020) requires defining a threshold dependent on the system concentration and excluded volume effects. The search radius ϵd_p , where ϵ is the contact distance between centroids of adjacent pairs of particles normalised by the mean particle diameter, is determined by analysing a low- Ca case where tightly bound clusters and a few single particles coexist. We then plot the nearest-neighbour distance for each particle in ascending order and identify the transition point where the distribution flattens (figure 1a). The results are only weakly dependent on the precise value of ϵ . This corresponds to an inter-particle gap much smaller than d_p and comparable to the expected thickness of a lubrication layer between capillarity-bonded particles.

Figure 1(b) displays a resulting example of cluster detection at $Ca = 0.33$ and $\phi = 0.44$ based on $\epsilon = 1.20$, our choice for this particle type based on the nearest-neighbour distance distribution. We apply the same value of ϵ to all cases with the same type of particles: a search radius of $1.25d_p$ is used for SL and DL1 and $1.20d_p$ for DL2.

To assess turbulence intensity under different electromagnetic forcing, we perform separate particle image velocimetry (PIV) experiments where the fluid is exclusively laden with polyethylene microspheres as tracers ($d_p = 75 - 90 \mu\text{m}$, Cospheric UVPMS-BG-1.00). These stay at the free surface (SL) or at the liquid–liquid interface (DL), similarly to the millimetric particles. We calculate the Reynolds number $Re \equiv u_{rms,f} L_F / \nu$ based on

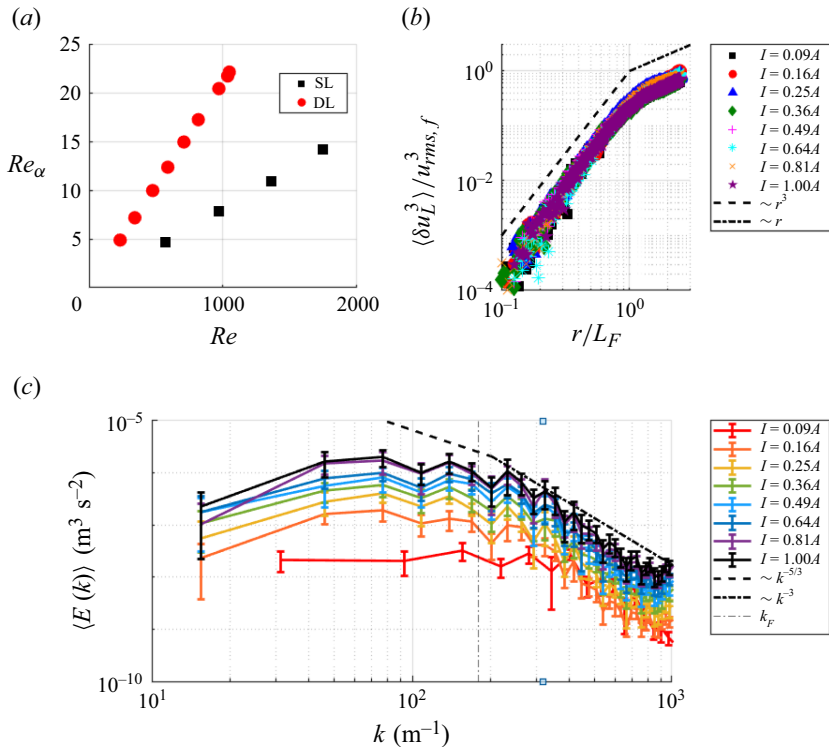


Figure 2. (a) Range of Reynolds numbers Re and Re_α for the SL (black) and DL (red) configurations in this study. (b) Normalised third-order longitudinal structure function, $\langle \delta u_L^3 \rangle / u_{rms,f}^3$, and (c) energy spectrum, $\langle E(k) \rangle$, at varying levels of forcing for the DL configuration.

$u_{rms,f}$, which is varied by adjusting the electrical current from 0.09 to 1.00 A. The level of forcing falls within the turbulent regime (Shin *et al.* 2023), with Kolmogorov scales η comparable to d_p (table 1). The outer-scale Reynolds number $Re_\alpha = u_{rms,f} / (\alpha L_F)$, where α is the friction coefficient, equals or exceeds the approximate threshold $Re_\alpha \approx 5$ (figure 2a) which ensures fully developed 2-D turbulence (Shin *et al.* 2023). The scaling of the third-order longitudinal structure function $\langle \delta u_L^3 \rangle$ exhibits the expected transition from $\sim r^3$ to $\sim r$ for separations $r \approx L_F$ (figure 2b), while the energy spectrum is consistent with the scaling $E \sim k^{-3}$ in the wavenumber range $k > k_F$, where $k_F = 2\pi / L_F$ (figure 2c); see Boffetta & Ecke (2012). The limited size of the system does not allow to ascertain the expected scaling $E \sim k^{-5/3}$ for $k < k_F$.

To provide a baseline for comparing the effects of particle–particle and particle–fluid interactions, we use random sequential adsorption (RSA) to virtually distribute non-overlapping circles in the two-dimensional (2-D) domain (Evans 1993). The circle sizes are drawn from a normal distribution matching the particle size distribution in our experiments (approximately Gaussian with standard deviation listed in table 1). We generate random configurations up to $\phi = 0.54$, close to the saturation coverage of 0.547 (Hinrichsen, Feder & Jøssang 1990). This RSA approach mimics a scenario devoid of any forcing length scale and inter-particle interactions (except for the excluded volume). Note that our DBSCAN clustering criterion – using the same threshold ϵ and a minimum requirement of four neighbours – is applied consistently to the RSA-generated configurations.

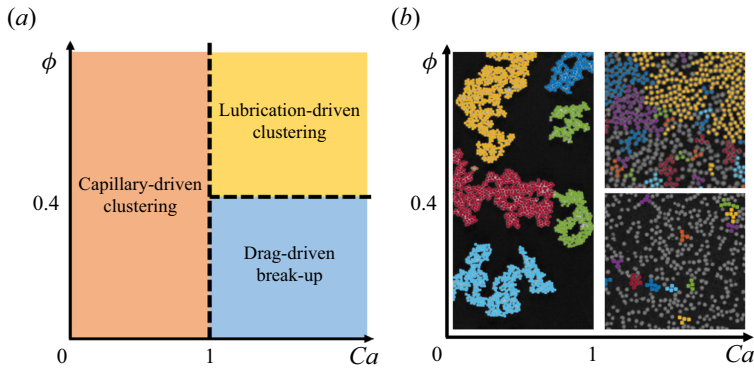


Figure 3. (a) Schematic of the three distinct clustering/break-up regimes within the $Ca - \phi$ phase space, adapted from Shin & Coletti (2024). (b) Examples of detected clusters from each regime. Particles within the same cluster are indicated with the same colour.

3. Results

As we demonstrated in Shin & Coletti (2024), the behaviour of the particles at the fluid interface is governed by the interplay of capillary, drag and lubrication forces. The ratio between those defines a $Ca - \phi$ phase space that captures different regimes of clustering and particle kinetic energy. Capillarity act as a cohesive mechanism between particles, and it is counteracted by viscous drag which disrupts cluster formation, especially in turbulent flows with locally high strain rates. For large Ca , the drag dominates promoting cluster break-up, particularly at relatively low (henceforth, moderately dense) concentrations. Conversely, when both ϕ and Ca are large, lubrication prevents particles from separating, allowing for large and stable clusters that move relatively slowly. Quantitatively, we identify three distinct regimes in the $Ca - \phi$ space: (i) capillary-driven clustering for $Ca < 1$, (ii) drag-driven break-up for $Ca > 1$ and $\phi < 0.40$ and (iii) lubrication-driven clustering for $Ca > 1$ and $\phi > 0.40$ (figure 3).

3.1. Cluster properties

3.1.1. Clustering fraction and length scale

The fraction of particles forming clusters, denoted as χ_{cl} , is a key metric for understanding how the tendency to aggregating evolves across different flow regimes. This is defined as the number of particles contained in clusters, normalised by the total particle count. Figure 4(a) depicts χ_{cl} as a function of Ca at various ϕ . As already discussed in Shin & Coletti (2024), χ_{cl} increases with decreasing Ca (as capillarity prevails over drag) and increasing ϕ (as lubrication prevails over drag). Moreover, for increasing Ca at a given ϕ , χ_{cl} approaches the level obtained in the synthetic data by RSA (dotted line). This implies that, when the fluid turbulence is sufficiently high, the statistical proximity of non-overlapping particles is largely responsible for the observed trend.

Figure 4(b) shows how the mean cluster length scale depends on Ca and ϕ . To avoid biases induced by the large number of small clusters, we define the weighted-average radius as

$$\langle R_g \rangle_w \equiv \frac{\sum_i n_{p,i} R_{g,i}}{\sum_i n_{p,i}}, \tag{3.1}$$

where $R_{g,i}$ is the radius of gyration of the i th cluster and $n_{p,i}$ is the number of particles forming it. At low Ca , particles are heavily influenced by strong attractive capillary forces

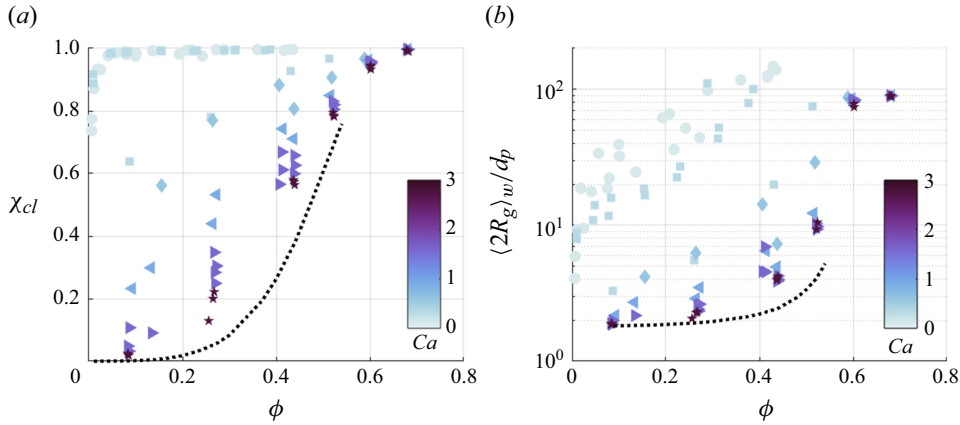


Figure 4. (a) Clustered particle fraction (χ_{cl}) as a function of areal fraction (ϕ) across different capillary numbers (Ca). (b) Normalised cluster size ($\langle 2R_g \rangle_w / d_p$) as a function of ϕ at various Ca levels. In each case, the dotted line represents the clustering fractions from random configurations for the respective ϕ values, established through RSA up to $\phi = 0.54$.

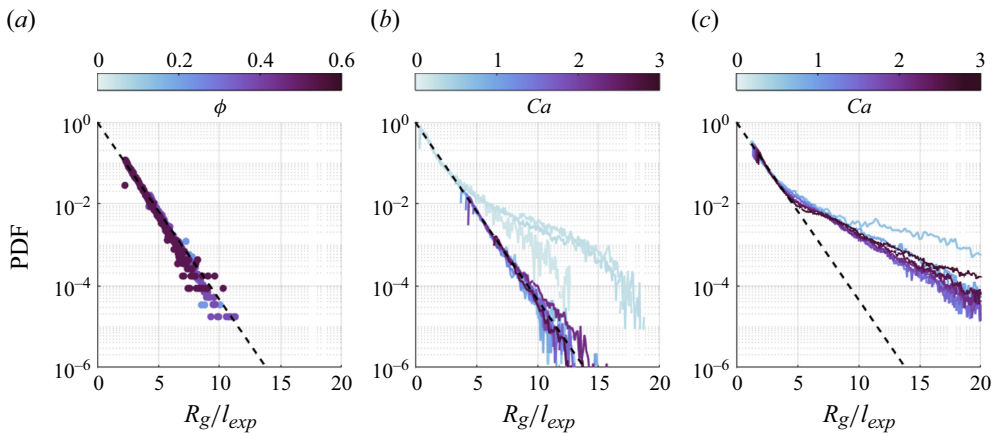


Figure 5. Probability density functions (PDFs) of the cluster size, R_g , normalised by the exponential decay length, (l_{exp}): (a) RSA-generated random configurations at $\phi = 0.27, 0.44$ and 0.53 . The corresponding values of l_{exp}/d_p are $0.20, 0.33$ and 0.87 , respectively. (b) The PDFs at $\phi = 0.27$ for various experimental capillary numbers: $Ca = 0.16, 0.23, 0.29, 0.87, 1.22, 1.51, 1.82, 2.10, 2.49$ and 2.69 , with the corresponding values of $l_{exp}/d_p = 5.66, 4.16, 3.76, 0.41, 0.37, 0.33, 0.29, 0.32, 0.25$ and 0.21 , respectively. (c) The PDFs at $\phi = 0.53$ for $Ca = 0.59, 0.87, 1.22, 1.51, 1.82, 2.10, 2.49$ and 2.69 with the corresponding values of $l_{exp} = 1.17, 1.00, 1.00, 0.95, 0.88, 0.83, 0.79$ and 0.74 . The black dashed line in each panel represents an exponential decay, $\exp(-R_g/l_{exp})$.

exceeding the disruptive effect of drag, leading to extended clusters. These can grow larger than a typical eddy size L_F , comprising hundreds of particles. With increasing Ca , these objects have higher chance of being exposed to extensional strain exceeding the capillarity, leading to more frequent break-up and thus smaller aggregates. Again, with increasing Ca the radius obtained by RSA is approached. Overall, both χ_{cl} and $\langle R_g \rangle_w$ indicate that, when the turbulent forcing is intense and $Ca \gg 1$, the clustering is increasingly governed by the stochastic adjacency of particles, rather than inter-particle interactions.

The PDFs of R_g offer further insight into how the clustering dynamics changes across regimes. Figure 5(a) shows that clusters formed by RSA exhibit an exponential

distribution, independently of ϕ . An exponential fit of the probability $p(R_g) \sim \exp(-R_g/l_{exp})$, applied to the RSA data as well as to experimental data that exhibit exponential decay, defines a characteristic length l_{exp} used to normalise the distributions in the different scenarios. Moderately dense systems (figure 5b) exhibit a transition with varying Ca : in the capillary-driven clustering regime ($Ca < 1$) the cluster radius PDFs possess long tails, with significant probability of large aggregates spanning the entire domain; while in the drag-driven break-up regime ($Ca > 1, \phi < 0.40$) drag disrupts the large clusters and the distribution gradually approaches the RSA behaviour. This observation supports the view that the clustering dynamics in moderately dilute systems is predominantly influenced by the random proximity of particles.

The scenario is different for denser systems (figure 5c). Here, both in the capillarity-driven regime ($Ca < 1$) and in the lubrication-driven clustering regime ($Ca > 1, \phi > 0.40$), the decay of the PDFs is much slower compared with RSA. This implies that the formation of very large clusters cannot be explained by excluded volume effect at high concentration, and are instead sustained by lubrication forces. At even higher concentrations, few large clusters percolate through the whole system. This scenario is discussed in the next section.

3.1.2. Cluster percolation and self-similarity

Dense particle systems are known to exhibit sharp transitions to a percolating state when their concentration increases above a threshold. In such a state, exceptionally large clusters are formed that span the entire domain. The threshold is system-dependent: for example, Shen, O'Hern & Shattuck (2012) found a critical area fraction $\phi^* = 0.549$ by simulating periodic 2-D layers of frictionless particles under compression, while the experiments of Alicke, Stricker & Vermant (2023) found $\phi^* = 0.3 - 0.36$ for particle layers under shear and compression.

The present system also exhibits a transition to a percolating state. This is illustrated in figures 6(a) and 6(b), where instantaneous realisations are shown for two representative cases at $Ca = 0.33$. While both have comparable concentrations $\phi = 0.44$ and 0.53 , only the latter displays percolating clusters. The transition is quantified in figure 6(c), plotting the percolation fraction χ_p (number of imaging frames featuring at least one cluster percolating through the whole field of view, divided by the total number of acquired frames) as a function of ϕ , for a representative value of $Ca = 0.33$. While we do not vary ϕ finely enough to identify a precise threshold ϕ^* , the transition appears relatively sharp. Visual inspection also confirms that the formation of a percolation cluster is hindered by increasing Ca , which favours more homogeneous patterns (figure 6d).

The trend across the parameter space is summarised in figure 6(e). For $Ca \ll 1$, we estimate $\phi^* \sim 0.4 - 0.5$, comparable to classic configurations of compressed/sheared particle layers (Alicke *et al.* 2023). On the other hand, for $Ca \geq 1$, the threshold is significantly higher, $\phi^* \sim 0.55 - 0.6$. This is consistent with the notion that percolation naturally emerges in self-similar systems, where the influence of a preferential scale characterising the pattern is weak or absent (Aharony & Stauffer 2003). At large Ca , the flow increasingly imposes the forcing length scale L_F that disrupts system-spanning clusters, and percolation can only be attained at the largest concentrations. In particular, as we showed in Shin & Coletti (2024), for $Ca > 1$, the typical cluster size exceeds L_F only for areal fractions above $\phi \sim 0.55$ (which we now identify as the approximate percolation threshold in this regime).

The dominant role of the forcing scale, as opposed to the larger scales where energy accumulates in Q2-D turbulence, was already stressed in studies of Lagrangian

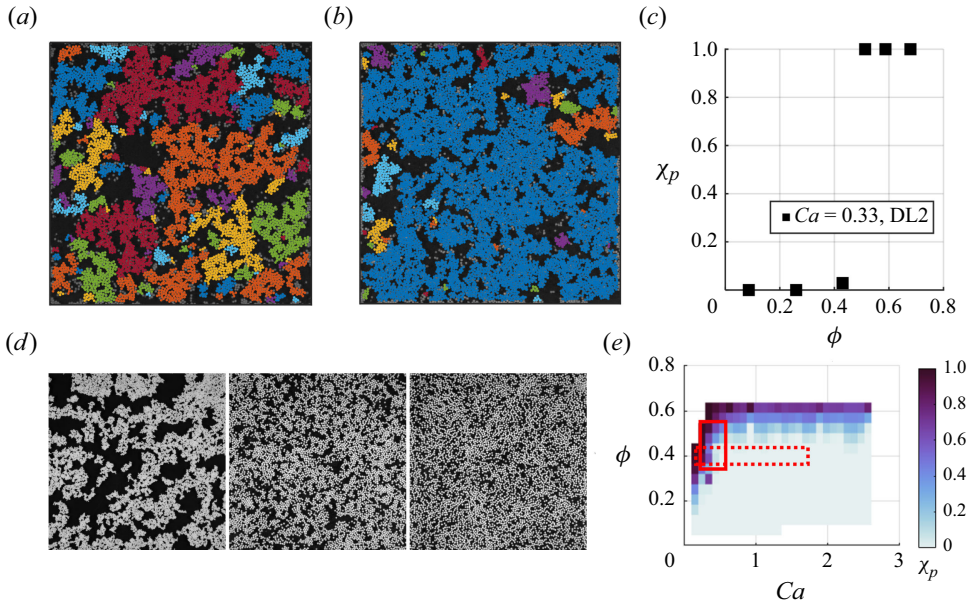


Figure 6. Snapshots with identified clusters at the same $Ca = 0.33$ but different areal fractions: (a) $\phi = 0.44$, and (b) $\phi = 0.53$. Particles within the same cluster are indicated with the same colour. (c) Fraction of frames χ_p where a system-spanning cluster is present as a function of ϕ at fixed $Ca = 0.33$. (d) Examples of cluster morphology for systems with $\phi \approx 0.44$ at different capillary numbers: $Ca = 0.29, 0.59$ and 1.82 (from left to right). At this ϕ , $Ca \ll 1$ entails the formation of a percolating structure, while higher Ca results in non-connected structures. (e) Value of χ_p in the $Ca - \phi$ space. Panels (a) and (b) correspond to the points inside the red solid rectangle, and panel (d) corresponds to cases inside the red dotted rectangle.

dispersion (Xia *et al.* 2013, 2019). For both particle clustering and dispersion, such a role is likely rooted in the persistent nature of eddies of size L_F (see discussion in Xia *et al.* 2013). On the other hand, when inter-particle attraction becomes dominant, cohesive clusters much larger than L_F appear. One may hypothesise that those might be related to commensurately large-scale fluid motions, either due to the inverse cascade or engendered by the influence of the clusters themselves on the flow. To investigate this possibility, we define the Eulerian velocity autocorrelation $\Gamma_E(r) = \langle \mathbf{u}(\mathbf{x}_0, t) \cdot \mathbf{u}(\mathbf{x}_0 + \mathbf{r}, t) \rangle_{\mathbf{x}_0, t} / \langle \mathbf{u}(\mathbf{x}_0, t) \cdot \mathbf{u}(\mathbf{x}_0, t) \rangle_{\mathbf{x}_0, t}$ and compare it for both particles and tracers. This is shown in figure 7 for the representative case $Ca = 2.69$ and $\phi = 0.62$. It highlights how, even when particles form large percolating clusters, the correlation scale of their motion matches that of the fluid flow (approximately $0.5L_F$, see Shin *et al.* 2023). We deduce that the emergence of system-spanning clusters is not related to fluid motions at scales larger than L_F .

In order to further characterise the present system within the percolation framework, we analyse the cluster size distributions. Unlike in sub-§ 3.1.1 where we focused on a geometric scale, here, we focus on the size, intended as the number of particles n_p contained in each cluster. In particular, we evaluate the cluster number density $f(n_p)$, namely the number density of clusters of size n_p per unit area. In 2-D self-similar particle systems (e.g. patterns of droplets condensing on surfaces (Stricker *et al.* 2022)), we expect $f(n_p) \sim (n_p/n_{p,max})^{-\xi} (n_{p,max}A_p)^{-\theta}$, where $n_{p,max}$ is the size of the largest cluster in the distribution, ξ is the so-called polydispersity exponent characterising the scaling range, $A_p = \pi d_p^2/4$ is the projected area of a particle and θ is a trivial exponent depending on

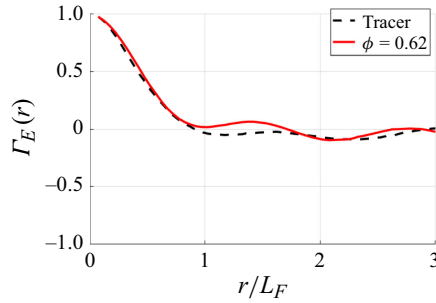


Figure 7. Examples of the Eulerian velocity autocorrelation for the DL configuration. The dashed line represents tracers ($Re = 1047$), while the red line corresponds to a dense suspension of particles at the same level of forcing ($Ca = 2.69$ and $\phi = 0.62$), where they form a large, system-spanning cluster.

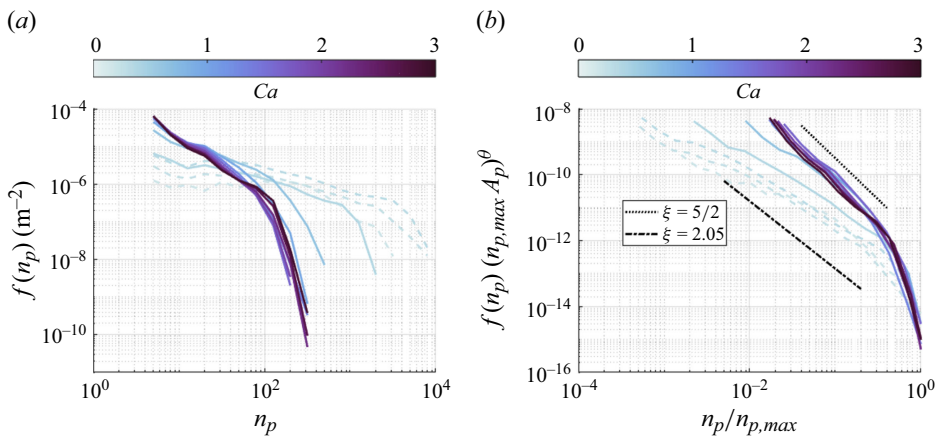


Figure 8. (a) Cluster size distributions for a particle area fraction $\phi \approx 0.44$ at different capillary numbers Ca . Here, n_p is the number of particles within a cluster, characterising the cluster size and $f(n_p)$ is the areal number density of clusters of size n_p . Dashed lines denote experiments in the SL configuration, while solid lines are from the DL2 set-up. (b) Normalised form of the same data, where $n_{p,max}$ is the size of the largest cluster, $A_p = \pi d_p^2/4$ is the projected area of a particle and $\theta = 1$ is a trivial exponent from dimensional analysis. Two limiting values of the polydispersity exponents, $\xi = 2.05$ (dash-dot) and $\xi = 5/2$ (dotted), which correspond to the predicted Fisher’s exponent (Fisher 1967), are indicated.

the dimensionality of the system, which has here the value of 1 to guarantee dimensional consistency.

Figure 8(a) reports $f(n_p)$ for cases of comparable areal fraction, $\phi \sim 0.44$, displaying self-similar scaling ranges with a polydispersity exponent that varies with Ca (considering comparable or higher concentrations, not shown for brevity, leads to analogous conclusions). To extract the polydispersity exponents, we rescale $f(n_p)$ in figure 8 to have $f(n_p)(n_{p,max} A_p)^\theta$, which is expected to scale as $(n_p/n_{p,max})^{-\xi}$.

For $Ca < 1$, the scaling range is broad and ξ is somewhat smaller than but comparable to the value of 2.05 characterising 2-D percolation, as observed in randomly generated clusters on regular lattices (Stauffer 1979). The discrepancy may be attributed to finite size effects.

This indicates that, in the capillary-driven clustering regime, the present system shares similarities (at least topologically) with classic percolating particle systems. For large

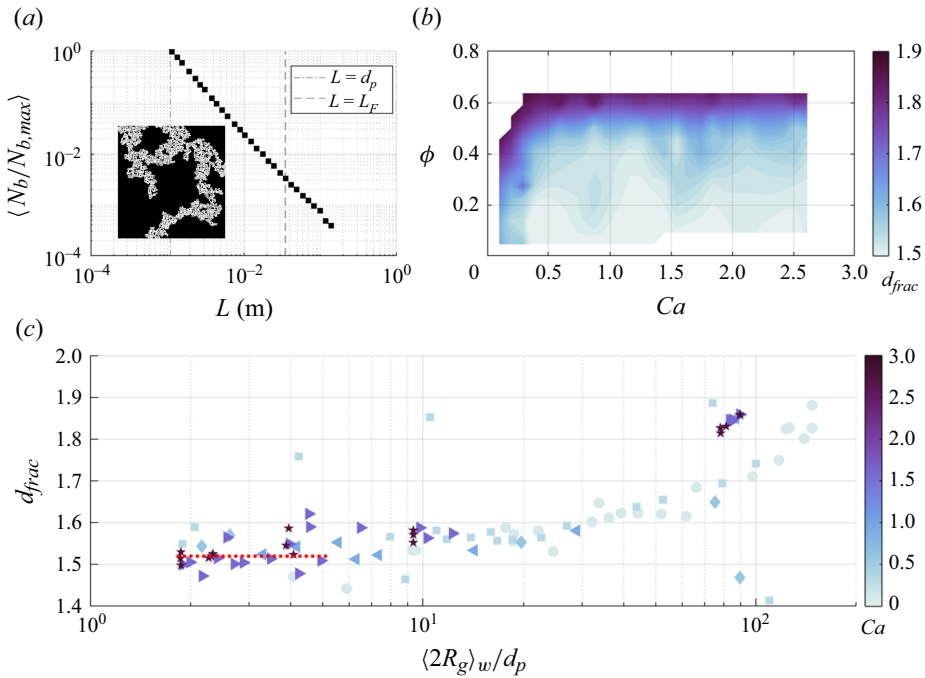


Figure 9. Fractal dimension d_{frac} obtained via the box-counting method. (a) An example of normalised box count as a function of box side length for a cluster (inset), (b) d_{frac} mapped in the $Ca - \phi$ space and (c) d_{frac} as a function of the mean cluster size. The red dotted line indicates the mean d_{frac} from varying ϕ values obtained via RSA.

capillary numbers $Ca > 1$, on the other hand, the scaling range is narrower as the forcing hinders the formation of self-similar structures. Over approximately a decade, however, the size distribution is consistent with a polydispersity exponent $\xi = 5/2$. This corresponds to the well-known prediction derived by Fisher (1967) for a coagulation process under the assumption that each agglomerate has equal probability of interacting with any other. Such a condition is typically not satisfied in standard percolation processes, leading to shallower exponents (Hoshent *et al.* 1979; Stauffer 1979). We therefore hypothesise that, in the present configuration, the forcing by the underlying turbulence contributes to randomising the system, effectively restoring the validity of Fisher’s assumption. We remark that this is the first observation of a percolation transition in turbulent particle suspensions, and its detailed properties deserve further investigation.

3.1.3. Clusters’ internal structure

The different mechanisms at play in the $Ca - \phi$ space can affect not only the clusters’ size but also their internal structure. Even though particle patterns may not be strictly self-similar, an operational definition of fractal dimension d_{frac} can be useful to quantify the compactness and complexity of their geometry. To estimate it, we select in each frame the cluster containing the largest number of particles, and we reconstruct its binary image based on the centroids and diameter of its particles. We then apply to it the box-counting method (Monchaux, Bourgoïn & Cartellier 2012; Baker *et al.* 2017), with L the box size (figure 9a). The data are normalised by the maximum count $N_{b,max}$ obtained from the smallest box size ($L = O(d_p)$) yielding a plot of $N_b/N_{b,max}$ as a function of L , where N_b

is the number of boxes that cover the binarised cluster. The normalised curves from all analysed clusters are averaged to extract d_{frac} by linear fitting in logarithmic scale.

Figure 9(b) maps the fractal dimension in the $Ca - \phi$ space. Similarly to χ_{cl} and $\langle R_g \rangle_w$ previously discussed, d_{frac} drops sharply in moderately dense suspensions ($\phi < 0.40$) within a narrow range of $Ca < 1$. Further increasing Ca leads to d_{frac} flattening around 1.5, close to the baseline value of 1.52 ± 0.2 from RSA which exhibits negligible ϕ dependence. When $Ca > 1$, the contour lines become largely horizontal, signalling a major role of ϕ . The lubrication-driven clusters are indeed compact, the particles filling the open spaces in their internal structure.

We now consider how d_{frac} varies with $\langle R_g \rangle_w$ (figure 9c). While small clusters (up to $\langle R_g \rangle_w/d_p = O(10)$) exhibit values of d_{frac} similar to those generated by RSA, for larger ones d_{frac} increases with size, tending to (although never reaching) the value of 2 characteristic of round (non-fractal) objects. For large $\langle R_g \rangle_w/d_p = O(10^2)$, d_{frac} is significantly lower for $Ca < 1$. This indicates a convoluted structure, which can be the result of hit-and-stick collisions, frequent when the capillary forces are too strong to be overcome by drag. In contrast, clusters at $Ca > 1$ have a more dynamic composition, with particles continuously joining and leaving the aggregate due to relatively weaker cohesive forces. Thus, we can draw an analogy between the cluster formation at low Ca and the diffusion-limited cluster aggregation (DLCA) which is known to result in more open (less compact) clusters (Meakin 1983; Lazzari *et al.* 2016). Notably, unlike DLCA of colloids driven by Brownian diffusion, our system employs non-Brownian particles driven by the underlying turbulent flow. In systems exhibiting aggregation of particles in turbulence, the fractal dimension of the aggregates has been evaluated both experimentally (e.g. Maggi, Mietta & Winterwerp 2007) and numerically (e.g. Zhao *et al.* 2021). In particular, Zhao *et al.* (2021) provided empirical scaling for d_{frac} as a function of the key non-dimensional parameters. The present results qualitatively agree with their model, e.g. concerning the increase of d_{frac} with larger cluster size. A quantitative comparison, however, is hindered by the fact that the present configuration is quasi-two-dimensional.

A natural metric to assess the degree of ordering/packing inside clusters is the hexatic order parameter ψ_6 , which measures the local ordering based on the orientation of the particle's six nearest neighbours. For the particle j , it is defined as

$$\psi_{6,j} = \frac{1}{6} \left| \sum_{k=1}^6 \exp(i6\theta_{jk}) \right|, \quad (3.2)$$

where k is an index for the six nearest neighbouring particles, θ_{jk} is the angle between the reference direction and the line connecting the particle j and its neighbouring particle k .

We assess ψ_6 for all individual clustered particles, ranging between 0 (dislocations and disclinations) and 1 (hexagonal crystal). Figure 10(a) compares the PDFs of ψ_6 for the same $\phi = 0.44$ and two different Ca . It is clear that lower Ca yields higher probabilities of large ψ_6 values. Increasing Ca pushes the PDF towards lower ψ_6 values, approaching the distribution obtained by RSA at the corresponding area fraction.

We further consider the average hexatic order parameter over all clustered particles, $\langle \psi_6 \rangle$, in the $Ca - \phi$ space (figure 10b). This displays a similar trend to previously discussed metrics: it diminishes as the system transitions from the capillary-driven clustering to drag-driven regime, and increases transitioning to lubrication-driven clustering. Plotting $\langle \psi_6 \rangle$ as a function of ϕ (figure 10c) indicates how the high- Ca cases follow closely the values obtained by RSA. This indicates again that clusters formed under strong turbulence forcing tend to resemble those formed by a random process.

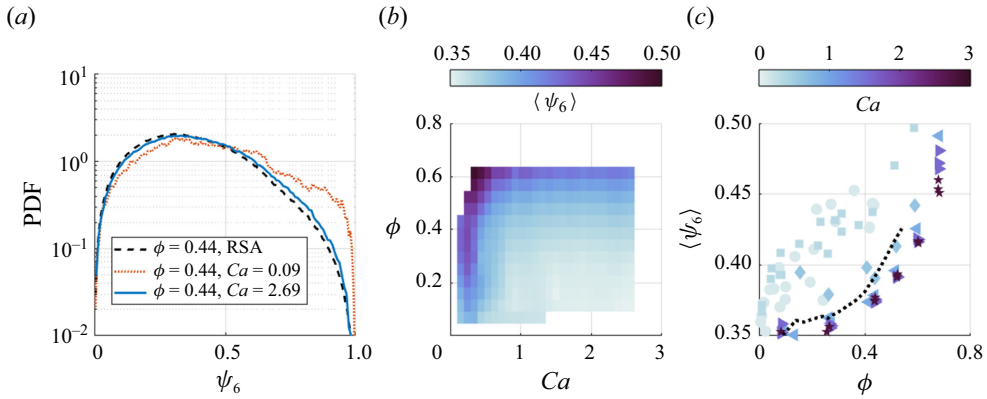


Figure 10. Hexatic order parameter (ψ_6) of the clustered particles. (a) The PDFs of ψ_6 at $\phi = 0.44$ but different Ca values: 0.09 (red) and 2.69 (blue). The black dashed line represents values from RSA for comparison. (b) Value of $\langle \psi_6 \rangle$ mapped in the $Ca - \phi$ space. (c) Value of $\langle \psi_6 \rangle$ as a function of ϕ across varying Ca . The black dashed line represents values obtained from RSA.

3.1.4. Cluster lifetime

The observation that clusters formed at low Ca are more compact than those at high Ca suggests that the former may also be longer lived. Verifying this hypothesis, and in general understanding the temporal dynamics of particle clusters within turbulent flows, requires estimating a cluster’s lifetime. The challenge, however, is represented by the dynamic nature of such entities where particles continuously join and escape.

Following Liu *et al.* (2020), we regard clusters in successive time steps as the same entity if they share the majority of their particles. This method mirrors the philosophical inquiry of the Ship of Theseus (see, e.g. Rea 1995). For example, consider two clusters A and B in two successive time steps. The fraction of forward-in-time connection is defined as the number of particles shared by A and B divided by the total number of particles in A; while the fraction of backward-in-time connection is the number of shared particles divided by the total number of particles in B. Clusters A and B are considered continuous manifestations of the same cluster if their fraction of forward- and backward-in-time connections both exceed 0.5, and their lifetime is the time during which such a condition is continuously verified. We then estimate the weighted-averaged cluster lifetime $\langle \tau_{cl} \rangle_w$ as

$$\langle \tau_{cl} \rangle_w \equiv \frac{\sum_i n_{p,i} \tau_{cl,i}}{\sum_i n_{p,i}}, \quad (3.3)$$

where $\tau_{cl,i}$ is the lifetime of the i th cluster.

To compare among different cases, the cluster lifetime is to be normalised by a time scale that reflects the particle–fluid dynamics. A natural choice is the eddy turnover time of the underlying flow, $L_F/u_{rms,f}$. This is verified by analysing the dispersion and stretching of the group of particles that initially belong to a cluster. We use singular value decomposition (Baker *et al.* 2017; Petersen, Baker & Coletti 2019), which identifies the first principal axis along the main direction of spread, the second axis being orthogonal to it. The corresponding singular values, s_1 and s_2 , are proportional to the spread of particle centroids along these axes. Figure 11(a) shows a representative example of temporal evolution of the normalised length scale $\langle R_g(t)/R_{g,0} \rangle$ and anisotropy $[s_2(t)/s_1(t)]/[s_{2,0}/s_{1,0}]$, where the subscript 0 indicates the time when the cluster is first

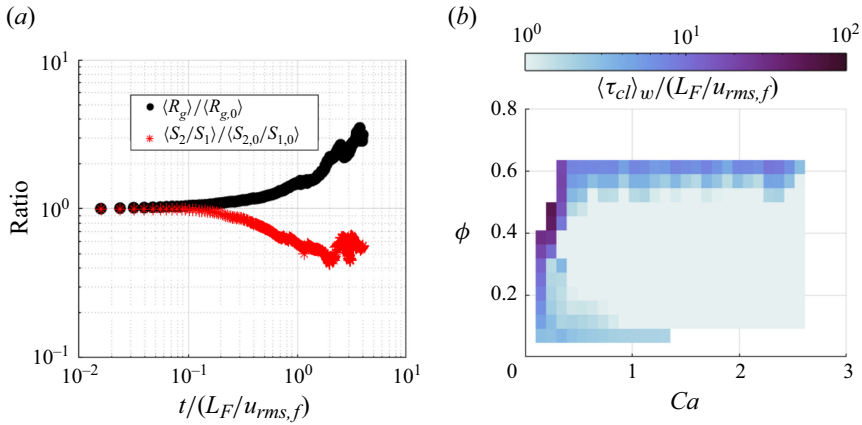


Figure 11. (a) Temporal evolution of the cluster size $\langle R_g(t)/R_{g,0} \rangle$ and cluster anisotropy $\langle S_2(t)/S_1(t) \rangle / \langle S_{2,0}/S_{1,0} \rangle$ for an example case with $Ca = 2.49$ and $\phi = 0.44$. (b) Contour map of the weighted average cluster lifetime $\langle \tau_{cl} \rangle_w$ normalised by the flow turnover time $L_F/u_{rms,f}$ across the $Ca - \phi$ space.

identified. The trend confirms that sizeable changes to the spatial organisation occur within a time $O(L_F/u_{rms,f})$.

For a given eddy turnover time, however, the cluster lifetime can be significantly larger or smaller depending on the balance of the forces at play. Figure 11(b) displays a contour map of the normalised cluster lifetime in the $Ca - \phi$ space. As expected, clusters have longer lifetimes for lower Ca , where cohesive capillary forces dominate. As Ca increases, particularly in the moderately dense regime ($\phi < 0.4$), clusters can live for just a fraction of the eddy turnover time before getting disrupted by the high strain rate of the intensely turbulent flow. On the other hand, in the denser regimes ($\phi > 0.4$) the cluster lifetimes can far exceed $L_F/u_{rms,f}$ irrespective of Ca . This is due to large clusters being brought about by excluded volume effects and kept together by lubrication. The particle dynamics within these large clusters, however, does vary substantially depending on Ca , as we show in the next section.

3.2. Particle dynamics

3.2.1. Single-particle dispersion

In Shin & Coletti (2024), we demonstrated how Eulerian properties of the particle motion, in particular their fluctuating kinetic energy, vary within the $Ca - \phi$ space. Here we focus on Lagrangian transport, which we first characterise in terms of the single-particle dispersion. It is worth remarking that the peculiar properties of 2-D turbulent flows impact the Lagrangian dispersion. In particular, as shown by Xia *et al.* (2013) and confirmed by Shin *et al.* (2023), the length scale that determines the dispersion process is the forcing scale L_F . This is at odds with the behaviour of 3-D turbulence, where dispersion is driven by the range of scales in which most energy reside. This characteristic was confirmed also in the transport of finite-size particles in Q2-D turbulence (Xia *et al.* 2019).

In the following, we consider the displacement \mathbf{r}_i of the i th particle from an initial position at time t_0 , and calculate the mean squared displacement (MSD) by averaging over all particles and initial times

$$\langle r^2(t) \rangle = \langle |\mathbf{x}_i(t_0 + t) - \mathbf{x}_i(t_0)|^2 \rangle_{i,t_0}, \quad (3.4)$$

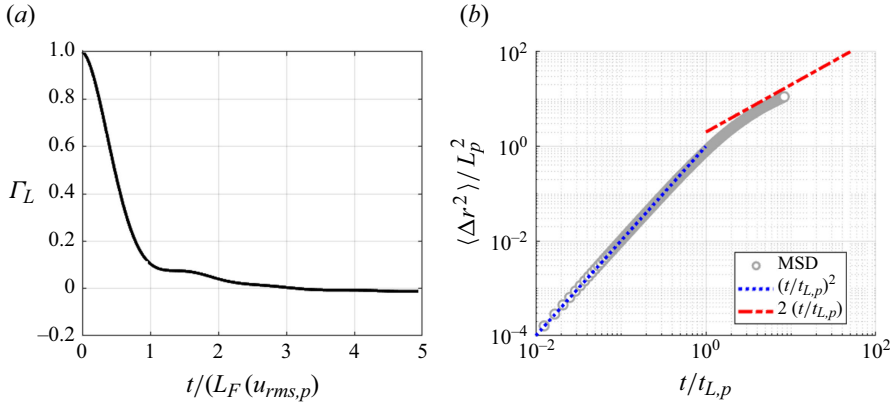


Figure 12. An example of (a) the Lagrangian velocity autocorrelation function (VACF) and (b) the MSD of particles for the case $Ca = 0.87$ and $\phi = 0.27$. The blue dotted line and red dash-dot line represent the short-term ballistic and long-term diffusive predictions, respectively, based on an exponentially decaying VACF with characteristic time scale $t_{L,p}$. The time is normalised by $t_{L,p}$, and the MSD is normalised by $L_p^2 = (u_{rms,p}t_{L,p})^2$.

where x_i represents the centroid position of the i th particle. As the Lagrangian velocity autocorrelation $\Gamma_L(t) = \langle \mathbf{u}_i(t_0) \cdot \mathbf{u}_i(t_0 + t) \rangle_{i,t_0} / \langle \mathbf{u}_i(t_0) \cdot \mathbf{u}_i(t_0) \rangle_{i,t_0}$ approximates an exponential decay of characteristic time t_L , one expects the classic scaling $\langle r^2(t) \rangle \approx u_{rms}^2 t^2$ for $t \ll t_L$, and $\langle r^2(t) \rangle \approx 2u_{rms}^2 t_L t$ for $t \gg t_L$, where u_{rms} is the root-mean-squared velocity. The approximately exponential decay of Γ_L for the turbulent flow was demonstrated in Shin *et al.* (2023) over a Lagrangian time scale of the flow that we term $t_{L,f}$. For the particles, Γ_L is shown by figure 12(a) in the example case $Ca = 0.87$ and $\phi = 0.26$. The characteristic time of the Lagrangian particle motion, $t_{L,p}$, is taken as the e-fold decay time of Γ_L and found to be comparable to the turnover time of the particle motion, $L_F/u_{rms,p}$. Figure 12(b) plots the MSD for the particles, confirming the expected short-time and long-time behaviours with a ballistic-to-diffusive transition around $t \sim t_{L,p}$.

The diffusive behaviour allows us to evaluate the long-term diffusivity associated with the particle motion as (Taylor 1922; Davidson 2015)

$$K_p = \frac{1}{2} \frac{d\langle r^2(t) \rangle}{dt} \approx u_{rms,p} L_p = u_{rms,p}^2 t_{L,p}, \quad (3.5)$$

where $L_p = u_{rms,p} t_{L,p}$ is a characteristic length scale of the particle motion. This is compared with the turbulent diffusivity of the fluid flow K_f , defining the normalised particle diffusivity

$$\frac{K_p}{K_f} = \frac{u_{rms,p}^2 t_{L,p}}{u_{rms,f}^2 t_{L,f}} = \frac{\langle E_{k,p} \rangle t_{L,p}}{\langle E_{k,f} \rangle t_{L,f}}, \quad (3.6)$$

where $\langle E_{k,p} \rangle$ and $\langle E_{k,f} \rangle$ are the mean kinetic energies of particles and fluid, respectively. Figures 13(a) and 13(b) map in the $Ca - \phi$ space the two factors: the particle-to-fluid ratio of fluctuating energy $\langle E_{k,p} \rangle / \langle E_{k,f} \rangle$, and the particle-to-fluid ratio of Lagrangian time scales $t_{L,p} / t_{L,f}$, respectively. Figure 13(a) reflects the observations made by Shin & Coletti (2024). In the capillary-driven clustering regime ($Ca < 1$) clusters can grow larger than the typical eddy size L_F , thus their motion is hindered as they filter out the energy of the smaller flow scales. In the drag-driven break-up regime ($Ca > 1$, $\phi < 0.4$), where the

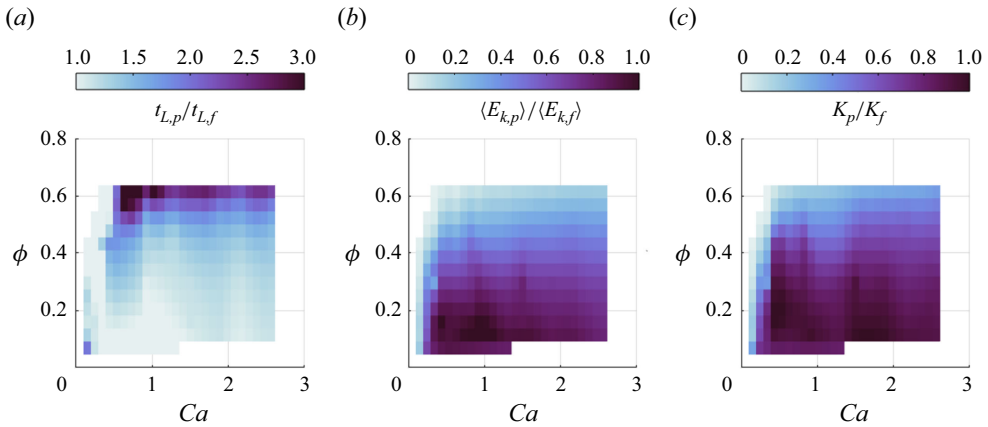


Figure 13. Contour maps in the $Ca - \phi$ space of (a) the ratio of Lagrangian time scales $t_{L,p}/t_{L,f}$, (b) the ratio of particle to fluid kinetic energy $\langle E_{k,p} \rangle / \langle E_{k,f} \rangle$ and (c) the normalised particle turbulence diffusivity K_p/K_f .

tendency to clustering is reduced, individual particles and small clusters have little inertia and thus possess a fluctuating energy comparable to the tracers. In the lubrication-driven clustering regime ($Ca > 1, \phi > 0.4$), the particle kinetic energy is largely dissipated by the interaction with adjacent particles. Figure 13(b) shows how, if a particle belongs to a large compact cluster, it exhibits a long-time-correlated motion as it moves collectively with other members of the cluster. This results in $t_{L,p}/t_{L,f}$ exceeding unity for dense concentrations, in particular in the lubrication-driven clustering regime. The particle diffusivity in figure 13(c) is the result of both competing trends: reduced energy and longer time correlation for large/compact clusters, and *vice versa*. Quantitatively, the trend of the fluctuating energy prevails, and the map of K_p/K_f in the $Ca - \phi$ space closely resembles that of $\langle E_{k,p} \rangle / \langle E_{k,f} \rangle$. In conclusion, the clustering fostered by capillarity and lubrication reduces the particles' ability to diffuse through the system.

3.2.2. Velocity structure functions

Pair statistics are a classic tool to reveal how particles move relatively to each other. In order to highlight the dynamics of the aggregates, we restrict our attention to pairs of particles belonging to the same clusters, although this does not change the trend with respect to the unconditioned data analysis. We begin by considering the longitudinal and transverse second-order velocity structure functions, defined respectively as

$$S_2^L(r) = \left\langle \left(\delta \mathbf{u}_{ij} \cdot \frac{\mathbf{r}_{ij}}{r} \right)^2 \right\rangle, \tag{3.7}$$

$$S_2^T(r) = \left\langle \left(\delta \mathbf{u}_{ij} - \delta \mathbf{u}_{ij} \cdot \frac{\mathbf{r}_{ij}}{r} \right)^2 \right\rangle. \tag{3.8}$$

Here, $\delta \mathbf{u}_{ij} = \mathbf{u}_j - \mathbf{u}_i$ is the velocity difference between the i th and j th particles whose separation vector is $\mathbf{r}_{ij} = \mathbf{x}_j - \mathbf{x}_i$, with $|\mathbf{r}_{ij}| = r$. The longitudinal component corresponds to $\delta \mathbf{u}_{ij}$ projected along the direction of \mathbf{r}_{ij} , which is responsible for the particles' separation, and the transverse component accounts for the element of $\delta \mathbf{u}_{ij}$ perpendicular to \mathbf{r}_{ij} , leading to rotation of the separation vector.

Figures 14(a–c) compares structure functions for both particles and tracers for the same level of forcing, normalised by $u_{rms,p}^2$ and $u_{rms,f}^2$, respectively. The three identified

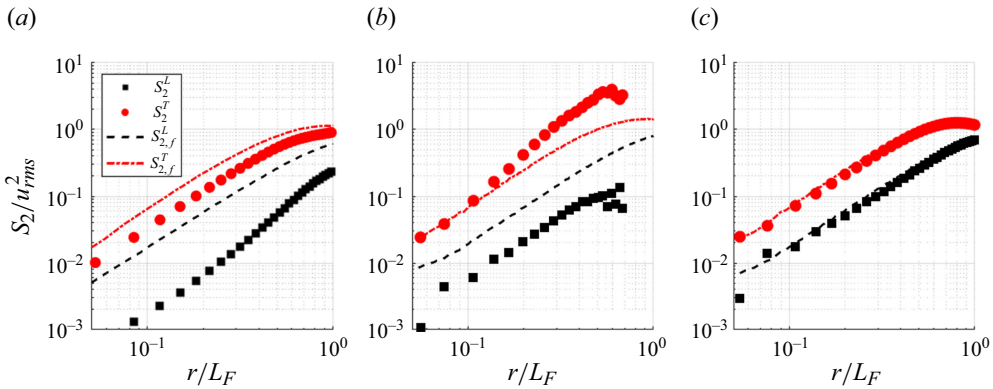


Figure 14. Examples of the second-order velocity structure functions (S_2) of particles from different experiments: (a) $Ca = 0.16$ and $\phi = 0.14$, (b) $Ca = 1.82$ and $\phi = 0.27$ and (c) $Ca = 2.69$ and $\phi = 0.62$. In each panel, S_2^L (black squares) and S_2^T (red circles) are normalised by $u_{rms,p}^2$. The dashed and dash-dot lines represent S_2^L and S_2^T of tracers at the same level of forcing, respectively, normalised by $u_{rms,f}^2$.

regimes display distinctly different behaviours. In the capillary-driven clustering regime (figure 14a), both S_2^L and S_2^T are lower than those of tracers. Particles are tightly bound by capillarity within compact clusters, thus they translate collectively with relatively small longitudinal velocity differences. The transverse component of the relative velocity is inhibited to a degree that depends on the cluster size, but in general much less so than its longitudinal counterpart. In the drag-driven break-up regime (figure 14b), clusters cannot be sustained in the region of high strain rate, thus they tend to reside in large vortex cores where they spin as quasi-rigid bodies. As those compact clusters spin, the particles in them that are separated by relatively large distances attain a rotational motion (with respect to each other) even faster than fluid parcels at equivalent separation. In those same clusters, on the other hand, inter-particle interactions limit the longitudinal separation rate. In the lubrication-driven clustering regime (figure 14c), particle adjacency imposed by excluded volume leads to the formation of large clusters spanning multiple eddies. While their lifetime is relatively long (see § 3.1.4), they are continuously deformed by the underlying turbulent flow, and their normalised S_2^L and S_2^T approach those of tracers.

3.2.3. Particle pair dispersion

Finally, we characterise the particle relative dispersion in a Lagrangian framework. To this end, we measure the mean squared separation (MSS) by tracking the evolution of the separation vector \mathbf{r}_{ij} between particle pairs as a function of time

$$MSS(t) = \langle |\mathbf{r}_{ij}(t_0 + t) - \mathbf{r}_{ij}(t_0)|^2 \rangle. \tag{3.9}$$

We focus on particle pairs that are initially adjacent, i.e. for which, at the initial time, $r_{ij,0} \sim d_p$.

To define the normalisation time scale, we first resort to the theory of 2-D turbulence. In the enstrophy cascade subrange, classical arguments for the separation law of particle pairs in smooth flows predict an exponential growth of the MSS at short times, with a characteristic time scale $t_\zeta = \zeta^{-1/3}$, where $\zeta \equiv \nu \langle |\nabla \omega|^2 \rangle$ is the enstrophy dissipation rate and ω is the vorticity (Jullien 2003). We estimate ζ by modelling the flow field as an array of Taylor–Green vortices (Shin *et al.* 2023)

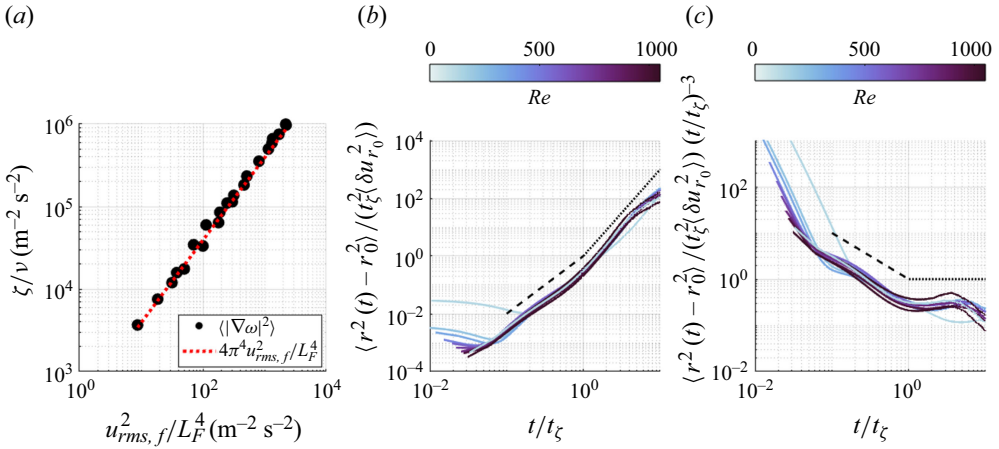


Figure 15. (a) Relationship between the enstrophy dissipation rate divided by the kinematic viscosity (ζ/ν) and $u_{rms,f}^2/L_F^4$. Markers are obtained from PIV analysis of tracer experiments, and the red dotted line represents the estimation based on Taylor–Green vortices with a slope of $4\pi^4$. (b) Examples of the MSS of tracers in the DL configuration at different levels of forcing, with an initial separation of 1.84 mm. The dashed and dash-dot lines indicate t^2 and t^3 scalings, respectively. (c) Compensated MSS, where the MSS is divided by $(t/t_\zeta)^3$, highlighting the t^3 scaling as a plateau.

$$\zeta/\nu = \langle |\nabla\omega|^2 \rangle = \frac{4\pi^4 u_{rms,f}^2}{L_F^4}. \quad (3.10)$$

This simplification yields quantitative agreement with the PIV measurements (figure 15a).

Based on this estimate, we approximate the characteristic time scale as $t_\zeta \approx (4\pi^4 \nu u_{rms,f}^2 / L_F^4)^{-1/3}$. For short times ($t \ll t_\zeta$), the MSS is primarily influenced by the initial velocity difference, $\langle \delta u_r^2(t) \rangle \approx \langle \delta u_{r_0}^2 \rangle$. We therefore rescale the MSS as $\langle |\mathbf{r}_{ij}(t_0 + t) - \mathbf{r}_{ij}(t_0)|^2 \rangle / (t_\zeta^2 \langle \delta u_{r_0}^2 \rangle)$, similar to Li *et al.* (2024) who studied pair-dispersion in free-surface turbulence, with t_ζ replacing their transition time t_D between ballistic and diffusive behaviours of the relative velocity δu .

Figure 15(b) presents normalised MSS curves from tracers in the DL configuration, with an initial separation $r_{ij,0} \sim d_p$. This is close to the range of initial separation of $2 - 4\eta$ that Tan & Ni (2022) proposed as an upper limit for observing the super-diffusive scaling $\langle |\mathbf{r}_{ij}(t_0 + t) - \mathbf{r}_{ij}(t_0)|^2 \rangle / \sim t^3$ in single-phase homogeneous turbulence. This scaling was originally proposed by Richardson (1926) based on a scale-dependent diffusivity, and later justified by Obukhov (1941) as consistent with Kolmogorov’s (1941) theory. According to the latter, the dissipation rate of the turbulent kinetic energy is the only governing parameter in the inertial range, which dimensionally leads to the super-diffusive scaling. Here, the MSS curves collapse well on the chosen normalisation. For $t/t_\zeta \ll 1$, we note that experimental limitations such as resolution constraints affect the precise measurement of very small relative displacements of nearby tracers. This is likely the cause of the weak decline in separation observed at low Reynolds numbers. For $t/t_\zeta > 1$, the MSS curves display the super-diffusive scaling, and this persists until the separation grows beyond L_F , where the dispersion becomes purely diffusive.

The t^3 -scaling range (highlighted by the compensated plots in figure 15c) is therefore limited by the scales of the system, and possibly by factors such as cross-scale contamination, which have made the super-diffusive regime particularly elusive (Bourgoin *et al.* 2006; Salazar & Collins 2009; Bitane, Homann & Bec 2012; Elsinga, Ishihara &

Hunt 2022; Tan & Ni 2022). The limited range over which the super-diffusive scaling is observed, and the fact that such an observation typically requires small initial separations (below the inertial range prescribed by Richardson–Obukhov theory) has created significant debate on the nature of the process in both 2-D and 3-D turbulence (Kellay & Goldburg 2002; Elsinga *et al.* 2022). This issue is, however, outside the scope of the present study: our interest is rather on how the particle dispersion compares with the fluid tracer dispersion, as we now discuss.

The observable width of the super-diffusive regime depends on the scale separation between the forcing scale L_F and the initial separation. For separations much larger than L_F , the behaviour ultimately becomes diffusive, with a corresponding time scale roughly given by $t_{L,p} \sim L_F/u_{rms,p}$. In our analysis, the temporal scale separation between the inertial (ballistic or super-diffusive) regime and the diffusive regime scales approximately as $t_{L,p}/t_\zeta \sim L_F^{-1/3}$, modulated by the velocity ratio $u_{rms,f}/u_{rms,p}$ at the given flow Re . Thus, increasing L_F would, in a purely temporal sense, slightly reduce the window over which super-diffusion is observed. Conversely, from a spatial perspective, it is crucial that L_F is significantly larger than the typical initial separation (which is lower bounded by the particle diameter d_p); indeed, our results indicate that, if the initial separation exceeds approximately $0.25L_F$, the t^3 -scaling is not apparent and replaced by ballistic scaling ($\sim t^2$). Moreover, when the particle velocity $u_{rms,p}$ is much lower than the fluid velocity $u_{rms,f}$ – as observed at high areal fractions – the effective temporal separation is enhanced, thereby extending the super-diffusive regime.

The relative dispersion of the particles is illustrated in figure 16 for different values of Ca and ϕ , again for $r_0 \sim d_p$. A dashed line showing the MSS of tracers for a representative case (weakly dependent on the forcing, as shown in figure 15) is included for reference. In the moderately dense case ($\phi = 0.27$, figure 16a), we observe slower initial dispersion at $t/t_\zeta < 1$, due to capillarity and lubrication inhibiting separation at small distances. Once particle pairs grow far enough apart that cohesive interactions become negligible, the curves at different Ca collapse and exhibit a super-diffusive scaling for over a decade, until the separation grows beyond L_F .

At $\phi = 0.71$ (figure 16b), the effect of Ca becomes more prominent. At $Ca \ll 1$, as the particle velocity is significantly slower than the fluid velocity (see figure 12a), it takes much longer than t_ζ for a pair to separate enough to break away from their mutual attraction. Conversely, at $Ca > 1$ particle separation occurs more rapidly and the super-diffusive regime is retrieved. This scaling of relative dispersion in such densely packed cases is striking, as most particles remain contained within a massively large, percolating cluster. This highlights the dynamic nature of clusters formed at high Ca , in contrast to the quasi-rigid clusters formed at low Ca . This change in behaviour is not captured by the analysis of cluster lifetime, which shows no noticeable trend with Ca at $\phi = 0.71$ (see figure 11b).

When using t_ζ for normalisation, the transition to the super-diffusive regime at dense concentrations occurs at different times. This is not surprising, as the fluid enstrophy is unlikely to be the governing factor at such high particle concentrations. We hypothesise that, for dense suspensions at high Ca (i.e. in the lubrication-driven clustering regime), the frequent inter-particle interactions via lubrication, rather than the fluid enstrophy, become the dominant mechanism governing the energy dissipation and in turn the relative dispersion. For each particle, the energy dissipation rate due to lubrication is $\varepsilon_{lub} \sim F_{lub}u_{rel}$, where F_{lub} is the lubrication force experienced by a particle moving with a velocity u_{rel} relative to its neighbour. Considering the particle number density per area $n = 4\phi/(\pi d_p^2)$ and the area density $\rho_A = \rho_f \delta$, where δ is the fluid layer thickness,

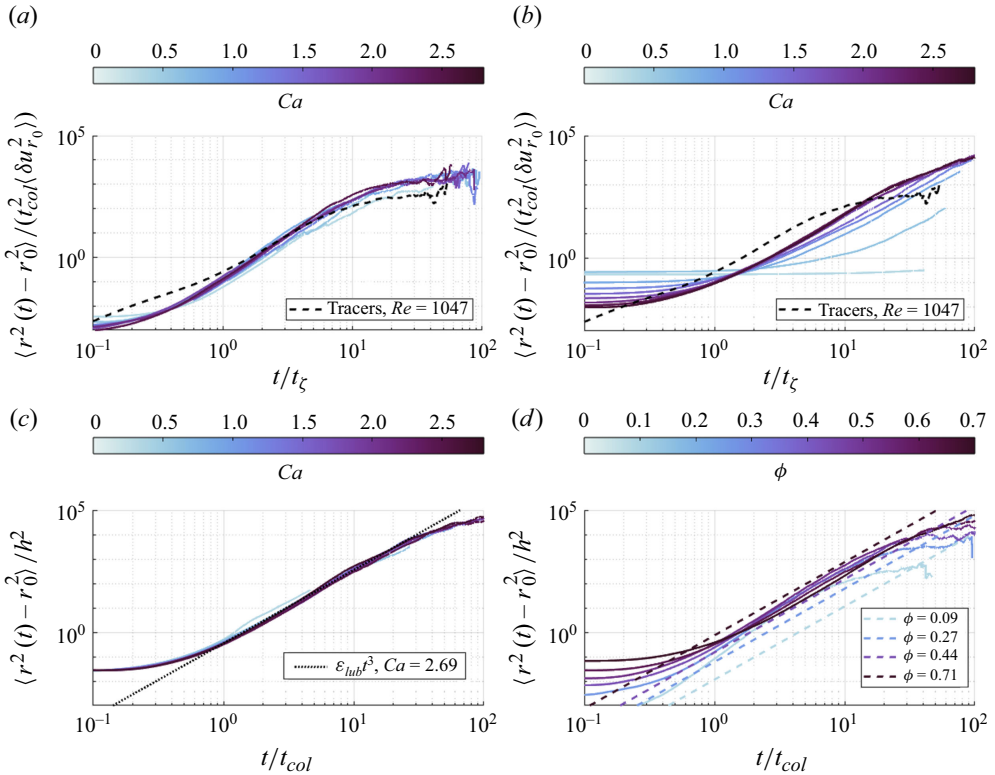


Figure 16. Examples of the MSS of particle pairs with an initial separation of $d_p = 1.84$ mm: (a) $\phi = 0.27$, and (b) $\phi = 0.71$. The dashed line corresponds to the MSS of tracers from the most turbulent flow in the experiments. (c) The MSS curves for high $\phi = 0.62$ across varying Ca values, with time normalised by the collision time scale $t_{col} = h/u_{rel}$ and MSS by h^2 . The dotted line indicates the MSS prediction by (3.12). (d) The MSS curves at $Ca = 2.49$ across different areal fractions, with lines indicating the MSS predictions by (3.12) at $\phi = 0.09, 0.27, 0.44$ and 0.71 (dash-dot), respectively.

the relevant short-range energy dissipation rate per unit mass can be approximated as

$$\varepsilon_{lub} \approx F_{lub} u_{rel} \frac{n}{\rho_A} \approx \frac{3\pi\mu d_p^2 u_{rel}^2}{2h} \frac{4\phi/(\pi d_p^2)}{\rho_f \delta} = \frac{6v_f u_{rel}^2}{\delta d_p} \frac{\phi}{[(\phi_{max}/\phi)^{0.5} - 1]}, \quad (3.11)$$

where $h = d_p [(\phi_{max}/\phi)^{0.5} - 1]$ is the mean surface-to-surface separation between neighbouring particles, with $\phi_{max} \approx 0.9064$ being the maximum areal fraction from the 2-D hexagonal close packing.

Under the assumption that ε_{lub} is the main governing parameter, dimensional arguments yield immediately $MSS \sim \varepsilon_{lub} t^3$, and therefore

$$MSS(t) \sim \varepsilon_{lub} t^3 \sim \frac{6v_f u_{rel}^2}{\delta d_p} \frac{\phi}{[(\phi_{max}/\phi)^{0.5} - 1]} t^3. \quad (3.12)$$

Here, the relevant length and time scale are associated with inter-particle collisions (meant in a general sense as direct interaction/contact), which we take as h and $t_{col} = h/u_{rel}$, respectively. Since the longitudinal second-order structure function $S_{2,p}^L/u_{rms,p}^2$ of particles in the lubrication-driven clustering regime shows excellent quantitative agreement with $S_{2,f}^L/u_{rms,f}^2$ of tracers (figure 14c), we approximate $u_{rel}(r) \sim$

$u_{rms,p}(S_{2,f}^L(r)/u_{rms,f}^2)^{0.5}$, evaluated at $r = h$. These length and time scales correspond to the distance and time over which a particle in a pair travels to encounter another neighbour whose centre is $h + d_p$ away from its own. For $\phi > 0.4$, the particles in densely packed suspensions are expected to forget their initial relative velocity through mutual interactions, with lubrication governing the decorrelation of their relative velocity.

This expectation is confirmed in figure 16(c,d), which plots the MSS curves for $\phi = 0.62$ with varying Ca values, and for $Ca = 2.49$ with varying ϕ values, respectively, normalised by t_{col} and h^2 . Figure 16(c) shows that this normalisation produces a tight collapse of the curves, which display a super-diffusive regime for $t > t_{col}$. Moreover, the super-diffusive MSS estimated for the highest Ca using (3.12), based on the assumption that lubrication is the dominant energy dissipation mechanism in dense cases (indicated with a dotted line), shows good agreement with the experimental curve. We stress that such a scaling argument is expected to apply within a pre-factor of order unity. The agreement between (3.12) and the experimental MSS implies that ε_{lub} takes on the role of the turbulent dissipation rate in single-phase flows.

To further inspect the role of short-range interactions in MSS across different concentrations, we plot the normalised MSS curves at $Ca = 2.49$ across varying ϕ values in figure 16(d). Dashed lines calculated using (3.12) indicate how the agreement progressively improves for increasing concentrations, as one transitions from the drag-driven break-up to the lubrication-driven clustering regime.

4. Conclusion

We have investigated the mechanisms governing particle clustering and dispersion in dense turbulent interfacial suspensions of non-Brownian, monodisperse spherical particles at immiscible fluid interfaces. Building upon the phase diagram in the capillary number (Ca) and areal fraction (ϕ) space constructed in our previous work (Shin & Coletti 2024), we have provided a comprehensive analysis of cluster properties and the particle dynamics across different regimes. By systematically varying the capillary number Ca and the areal fraction ϕ and analysing Lagrangian trajectories, we have characterised the clustering process via clustering fraction, cluster size distributions, percolation, fractal dimensions, hexatic order parameters and cluster lifetime. Additionally, we have explored the particle dynamics by examining single-particle dispersion, velocity structure functions and pair dispersion. Our findings reveal how the interplay between capillary forces, viscous drag and lubrication interactions dictates the behaviour of particles in these suspensions, leading to a distinct dynamics in different regions of the $Ca - \phi$ phase space. Specifically, concerning clustering:

- (i) In the capillary-driven clustering regime ($Ca < 1$), capillary attractions dominate over viscous drag, leading to the formation of large clusters through hit-and-stick type collisions. These clusters can grow to sizes even larger than the typical eddy size and exhibit relatively low fractal dimensions. That is, they have a fractal-like structure akin to what observed in diffusion-limited processes, resulting from particles aggregating via capillary forces without significant rearrangement.
- (ii) In the drag-driven break-up regime ($Ca > 1, \phi < 0.40$), increased turbulent fluctuations enhances viscous drag on the particles, which overcome capillary attraction. Particles tend to remain isolated or form small, short-lived clusters. The statistical properties of the clusters closely resemble those of random configurations generated by RSA processes: the clustering fraction, cluster size distributions and fractal dimensions approach those expected in random, non-interacting particle

arrangements, indicating that clustering arises primarily due to random proximity rather than cohesive forces.

- (iii) In the lubrication-driven clustering regime ($Ca > 1$, $\phi > 0.40$), frequent inter-particle interactions due to high particle concentration amplify the role of lubrication forces. Despite strong turbulent forcing, particles can form large, dynamically evolving clusters that can span the entire system and live much longer than the energetic eddies. Lubrication forces hinder particle separation, leading to densely packed, crystal-like structures.

Above a threshold level of concentration that depends on Ca , dense interfacial suspensions exhibit a percolation behaviour similar to what is observed in other non-turbulent particle systems. In particular, for $Ca < 1$ the cluster size distribution follows a self-similar shape found in randomly generated aggregates; while for $Ca > 1$ the behaviour resembles what predicted in coagulating agglomerates with equally probable interactions among all particles.

As for the particle dispersion, single-particle analysis shows that clustering reduces the diffusivity by lowering their kinetic energy significantly, despite an extended time correlation of the motion. The velocity structure functions indicate that particles in the capillary-driven clustering regime have a limited relative velocity due to the strength of the bonds. This is the case also in the drag-driven break-up regime, in which clusters are mostly found in vortex cores and are spun as quasi-rigid bodies. In the lubrication-driven clustering regime, the large long-lived clusters are deformed by the turbulent flow and the particle relative velocities behave similarly to those of tracers, although with a reduced magnitude.

Analysis of the relative dispersion shows how, in the capillary-driven clustering regime, adjacent particle pairs separate at initially slow rates due to strong capillary attraction. Once this is overcome by turbulent fluctuations, the dispersion becomes super-diffusive until the separation exceeds the large-eddy size. In the drag-driven break-up regime, pair dispersion closely resembles that of passive tracers in turbulence. In the lubrication-driven clustering regime, due to the frequent particle–particle interactions at high concentrations, the collision rate defines the relevant time scale. This results in a regime where, after breaking away from each other, initially adjacent particles separate super-diffusively, but proportionally to the energy dissipation rate of the lubrication forces. Therefore, even though in this regime the clusters appear densely packed, their internal structure at intermediate scales is continuously rearranging.

The present work is limited to Q2-D settings with specific particle types and sizes. Factors like particle shape, size polydispersity and varying interfacial properties (such as the presence of surfactants) could affect the nature of the capillary attraction. The moderate Re achieved may not capture all of the relevant dynamics present in more turbulent environments where the assumption of Stokesian dynamics could break down. Moreover, free-surface turbulent flows with sizeable depth are characterised by a compressible surface-velocity field which influences clustering and dispersion (Lovecchio, Marchioli & Soldati 2013; Li *et al.* 2024; Qi, Li & Coletti 2025). Future research is warranted to address these limitations by exploring a broader range of particle characteristics, interfacial conditions and flow regimes to test the generality of our findings. The combination of drag, capillarity and lubrication that we use to rationalise the present system is indeed a simplification which does not take into account higher-order effects. For example, recent studies have demonstrated the existence of fluctuation-induced hydrodynamic forces acting on single or multiple objects (Yang *et al.* 2019; Spandan *et al.*

2020; Davoodianidalik *et al.* 2022). While explicitly quantifying such forces is beyond the scope of the present work, future studies shall investigate their role directly.

Finally, the connections made with diffusion-limited aggregation, percolation theory and random particle systems emphasise potentially powerful links with research areas seldom intertwined with particle-laden fluid dynamics. For example, the present finding may be compared with the behaviour exhibited by active particles or colloids (Alert, Casademunt & Joanny 2022). These are driven by self-propulsion and thermal fluctuations, respectively, rather than turbulence in the carrier fluid. This results in qualitatively different behaviours, particularly concerning the inter-scale energy transfer. At high concentrations, on the other hand, the particle–particle interaction may prevail and similarities with the present class of dense turbulent suspensions might be expected. Any such analogy, however, is to be investigated by dedicated studies.

Funding. This work was supported by the Swiss National Science Foundation, grant number 200021-207318.

Declaration of interests. The authors report no conflict of interest.

REFERENCES

- AGRAWAL, N., CHOEIRI, G.H. & HOF, B. 2019 Transition to turbulence in particle laden flows. *Phys. Rev. Lett.* **122** (11), 114502.
- AHARONY, A. & STAUFFER, D. 2003 *Introduction to Percolation Theory*. Taylor & Francis.
- ALERT, R., CASADEMUNT, J. & JOANNY, J.-F. 2022 Active turbulence. *Annu. Rev. Condens. Matter Phys.* **13** (1), 143–170.
- ALICKE, A., STRICKER, L. & VERMANT, J. 2023 Model aggregated 2D suspensions in shear and compression: From a fluid layer to an auxetic interface? *J. Colloid Interface Sci.* **652**, 317–328.
- BAKER, L., FRANKEL, A., MANI, A. & COLETTI, F. 2017 Coherent clusters of inertial particles in homogeneous turbulence. *J. Fluid Mech.* **833**, 364–398.
- BAKER, L.J. & COLETTI, F. 2019 Experimental study of negatively buoyant finite-size particles in a turbulent boundary layer up to dense regimes. *J. Fluid Mech.* **866**, 598–629.
- BALACHANDAR, S. & EATON, J.K. 2010 Turbulent dispersed multiphase flow. *Annu. Rev. Fluid Mech.* **42** (1), 111–133.
- BITANE, R., HOMANN, H. & BEC, J. 2012 Time scales of turbulent relative dispersion. *Phys. Rev. E* **86** (4), 045302.
- BOFFETTA, G. & ECKE, R.E. 2012 Two-dimensional turbulence. *Annu. Rev. Fluid Mech.* **44** (1), 427–482.
- BOURGOIN, M., OUELLETTE, N.T., XU, H., BERG, J. & BODENSCHATZ, E. 2006 The role of pair dispersion in turbulent flow. *Science* **311** (5762), 835–838.
- BRANDT, L. & COLETTI, F. 2022 Particle-laden turbulence: progress and perspectives. *Annu. Rev. Fluid Mech.* **54** (1), 159–189.
- BROWN, E. & JAEGER, H.M. 2014 Shear thickening in concentrated suspensions: phenomenology, mechanisms and relations to jamming. *Rep. Prog. Phys.* **77** (4), 046602.
- CLIFT, R., GRACE, J.R. & WEBER, M.E. 2005 *Bubbles, Drops, and Particles*. Courier Corporation.
- DAVIDSON, P.A. 2015 *Turbulence: an Introduction for Scientists and Engineers*. 1st edn. Oxford University Press.
- DAVOODIANIDALIK, M., PUNZMANN, H., KELLAY, H., XIA, H., SHATS, M. & FRANCOIS, N. 2022 Fluctuation-induced interaction in turbulent flows. *Phys. Rev. Lett.* **128** (2), 024503.
- ELSINGA, G.E., ISHIHARA, T. & HUNT, J.C.R. 2022 Non-local dispersion and the reassessment of richardson’s t^3 -scaling law. *J. Fluid Mech.* **932**, A17.
- ESTER, M., KRIEGEL, H.P., SANDER, J. & XU, X. 1996 A density-based algorithm for discovering clusters in large spatial databases with noise. In *KDD’96: Proceedings of the Second International Conference on Knowledge Discovery and Data Mining*, pp. 226–231. AAAI.
- EVANS, J.W. 1993 Random and cooperative sequential adsorption. *Rev. Mod. Phys.* **65** (4), 1281–1329.
- FISHER, M.E. 1967 The theory of equilibrium critical phenomena. *Rep. Prog. Phys.* **30** (2), 615–730.
- FONG, K.O. & COLETTI, F. 2022 Experimental analysis of particle clustering in moderately dense gas–solid flow. *J. Fluid Mech.* **933**, A6.
- FULLER, G.G. & VERMANT, J. 2012 Complex fluid–fluid interfaces: rheology and structure. *Annu. Rev. Chem. Biomol. Engng* **3** (1), 519–543.

- GARBIN, V. 2019 Collapse mechanisms and extreme deformation of particle-laden interfaces. *Curr. Opin. Colloid Interface Sci.* **39**, 202–211.
- GUAZZELLI, E., MORRIS, J.F. & PIC, S. 2011 *A Physical Introduction to Suspension Dynamics*. Cambridge University Press.
- HINRICHSSEN, E.L., FEDER, J. & JØSSANG, T. 1990 Random packing of disks in two dimensions. *Phys. Rev. A* **41** (8), 4199–4209.
- HOEKSTRA, H., VERMANT, J., MEWIS, J. & FULLER, G.G. 2003 Flow-induced anisotropy and reversible aggregation in two-dimensional suspensions. *Langmuir* **19** (22), 9134–9141.
- HOGENDOORN, W., BREUGEM, W.-P., FRANK, D., BRUSCHEWSKI, M., GRUNDMANN, S. & POELMA, C. 2023 From nearly homogeneous to core-peaking suspensions: Insight in suspension pipe flows using MRI and DNS. *Phys. Rev. Fluids* **8** (12), 124302.
- HOGENDOORN, W. & POELMA, C. 2018 Particle-laden pipe flows at high volume fractions show transition without puffs. *Phys. Rev. Lett.* **121** (19), 194501.
- HOSHENT, J., STAUFFER, D., BISHOP, J.H., HARRISON, R.J. & QUINN, G.D. 1979 Monte carlo experiments on cluster size distribution in percolation. *J. Phys. A: Math. Gen.* **12** (8), 1285–1307.
- JULLIEN, M.-C. 2003 Dispersion of passive tracers in the direct enstrophy cascade: experimental observations. *Phys. Fluids* **15** (8), 2228–2237.
- KELLAY, H. & GOLDBURG, W.I. 2002 Two-dimensional turbulence: a review of some recent experiments. *Rep. Prog. Phys.* **65** (5), 845–894.
- KOLMOGOROV, A.N. 1941 The local structure of turbulence in incompressible viscous fluid for very large reynolds. *Dokl. Akad. Nauk SSSR* **30**, 301.
- LAZZARI, S., NICOUD, L., JAQUET, B., LATTUADA, M. & MORBIDELLI, M. 2016 Fractal-like structures in colloid science. *Adv. Colloid Interface Sci.* **235**, 1–13.
- LI, Y., WANG, Y., QI, Y. & COLETTI, F. 2024 Relative dispersion in free-surface turbulence. *J. Fluid Mech.* **993**, R2.
- LIU, Y., SHEN, L., ZAMANSKY, R. & COLETTI, F. 2020 Life and death of inertial particle clusters in turbulence. *J. Fluid Mech.* **902**, R1.
- LOVECCHIO, S., MARCHIOLI, C. & SOLDATI, A. 2013 Time persistence of floating-particle clusters in free-surface turbulence. *Phys. Rev. E* **88** (3), 033003.
- MADIVALA, B., FRANSAER, J. & VERMANT, J. 2009 Self-assembly and rheology of ellipsoidal particles at interfaces. *Langmuir* **25** (5), 2718–2728.
- MAGGI, F., MIETTA, F. & WINTERWERP, J.C. 2007 Effect of variable fractal dimension on the floc size distribution of suspended cohesive sediment. *J. Hydrol.* **343** (1-2), 43–55.
- MAGNAUDET, J. & MERCIER, M.J. 2020 Particles, drops, and bubbles moving across sharp interfaces and stratified layers. *Annu. Rev. of Fluid Mech.* **52** (1), 61–91.
- MATAS, J.-P., MORRIS, J.F. & GUAZZELLI, E. 2003 Transition to turbulence in particulate pipe flow. *Phys. Rev. Lett.* **90** (1), 014501.
- MEAKIN, P. 1983 Formation of fractal clusters and networks by irreversible diffusion-limited aggregation. *Phys. Rev. Lett.* **51** (13), 1119–1122.
- MONCHAUX, R., BOURGOIN, M. & CARTELLIER, A. 2012 Analyzing preferential concentration and clustering of inertial particles in turbulence. *Intl J. Multiphase Flow* **40**, 1–18.
- OBUKHOV, A. 1941 On the distribution of energy in the spectrum of turbulent flow. *Dokl. Akad. Nauk SSSR* **32**, 22.
- OLIVIERI, S., BRANDT, L., ROSTI, M.E. & MAZZINO, A. 2020 Dispersed fibers change the classical energy budget of turbulence via nonlocal transfer. *Phys. Rev. Lett.* **125** (11), 114501.
- PETERSEN, A.J., BAKER, L. & COLETTI, F. 2019 Experimental study of inertial particles clustering and settling in homogeneous turbulence. *J. Fluid Mech.* **864**, 925–970.
- PICANO, F., BREUGEM, W.-P. & BRANDT, L. 2015 Turbulent channel flow of dense suspensions of neutrally buoyant spheres. *J. Fluid Mech.* **764**, 463–487.
- PROTIÈRE, S. 2023 Particle rafts and armored droplets. *Annu. Rev. Fluid Mech.* **55** (1), 459–480.
- QI, Y., LI, Y. & COLETTI, F. 2025 Small-scale dynamics and structure of free-surface turbulence. *J. Fluid Mech.* **1007**, A3.
- REA, M.C. 1995 The problem of material constitution. *Philos. Rev.* **104** (4), 525–552.
- RICHARDSON, L.F. 1926 Atmospheric diffusion shown on a distance-neighbour graph. *Proc. R. Soc. Lond. A* **110** (756), 709–737.
- SALAZAR, J.P.L.C. & COLLINS, L.R. 2009 Two-particle dispersion in isotropic turbulent flows. *Annu. Rev. Fluid Mech.* **41** (1), 405–432.
- SHEN, T., O’HERN, S. & SHATTUCK, M.D. 2012 Contact percolation transition in athermal particulate systems. *Phys. Rev. E* **85** (1), 011308.

- SHIN, S. & COLETTI, F. 2024 Dense turbulent suspensions at a liquid interface. *J. Fluid Mech.* **984**, 1–6.
- SHIN, S., COLETTI, F. & CONLIN, N. 2023 Transition to fully developed turbulence in quasi-two-dimensional electromagnetic layers. *Phys. Rev. Fluids* **8** (9), 094601.
- SINGH, P. & JOSEPH, D.D. 2005 Fluid dynamics of floating particles. *J. Fluid Mech.* **530**, 31–80.
- SPANDAN, V., PUTT, D., OSTILLA-MÓNICO, R. & LEE, A.A. 2020 Fluctuation-induced force in homogeneous isotropic turbulence. *Sci. Adv.* **6** (14), eaba0461.
- STAUFFER, D. 1979 Scaling theory of percolation clusters. *Phys. Rep.* **54** (1), 1–74.
- STRICKER, L., GRILLO, F., MARQUEZ, E.A., PANZARASA, G., SMITH-MANNSCHOTT, K. & VOLLMER, J. 2022 Universality of breath figures on two-dimensional surfaces: an experimental study. *Phys. Rev. Res.* **4** (1), L012019.
- TAN, S. & NI, R. 2022 Universality and intermittency of pair dispersion in turbulence. *Phys. Rev. Lett.* **128** (11), 114502.
- TAYLOR, G.I. 1922 Diffusion by continuous movements. *Proc. Lond. Math. Soc.* **2** (1), 196–212.
- VOWINCKEL, B., ZHAO, K., ZHU, R. & MEIBURG, E. 2023 Investigating cohesive sediment dynamics in open waters via grain-resolved simulations. *Flow* **3**, E24.
- WANG, L.-P., PENG, C., GUO, Z. & YU, Z. 2016 Lattice boltzmann simulation of particle-laden turbulent channel flow. *Comput. Fluids* **124**, 226–236.
- XIA, H., FRANCOIS, N., PUNZMANN, H. & SHATS, M. 2013 Lagrangian scale of particle dispersion in turbulence. *Nat. Commun.* **4** (1), 2013.
- XIA, H., FRANCOIS, N., PUNZMANN, H. & SHATS, M. 2019 Tunable diffusion in wave-driven two-dimensional turbulence. *J. Fluid Mech.* **865**, 811–830.
- YANG, J., DAVOODIANIDALIK, M., XIA, H., PUNZMANN, H., SHATS, M. & FRANCOIS, N. 2019 Passive propulsion in turbulent flows. *Phys. Rev. Fluids* **4** (10), 104608.
- ZADE, S., COSTA, P., FORNARI, W., LUNDELL, F. & BRANDT, L. 2018 Experimental investigation of turbulent suspensions of spherical particles in a square duct. *J. Fluid Mech.* **857**, 748–783.
- ZHANG, K. & RIVAL, D.E. 2018 Experimental study of turbulence decay in dense suspensions using index-matched hydrogel particles. *Phys. Fluids* **30** (7), 073301.
- ZHAO, K., POMES, F., VOWINCKEL, B., HSU, T.-J., BAI, B. & MEIBURG, E. 2021 Flocculation of suspended cohesive particles in homogeneous isotropic turbulence. *J. Fluid Mech.* **921**, A17.